Ultra-Low-Loss Silicon Nitride Optical Beamforming Network for Wideband Wireless Applications

Yuan Liu , *Member, OSA*, Adam R. Wichman , *Member, IEEE*, Brandon Isaac, Jean Kalkavage, *Member, IEEE*,
Eric J. Adles, *Senior Member, IEEE*, Thomas R. Clark, *Senior Member, IEEE*,
and Jonathan Klamkin, *Senior Member, IEEE*

Abstract—Three optical ring resonator (ORR)-based integrated ultra-low-loss silicon nitride 1×4 optical beamforming networks (OBFNs) for millimeter-wave (mmW) beamsteering are reported. The group delay ripple of multi-ORR delay line was theoretically optimized and quantitatively studied by applying a genetic algorithm. The optimized 3-ORR delay true time delay (TTD) responses were experimentally achieved with 208.7 ps and 172.4 ps of delay tuning range for bandwidth of 6.3 GHz and 8.7 GHz, corresponding to a phase shift of 17.1π and 14.1π for 41 GHz mmW signal. The TTD performance of the 3-ORR delay line was also verified by controlling the delay of 3 Gbps data stream. A 22° beamsteering angle equivalent OBFN delay distribution was achieved for 41 GHz half-wavelength dipole antenna array. Both the theoretical analysis and experiments exhibit that the topology with one ring shared could balance the system complexity and TTD bandwidth well. Using heterodyne up-conversion technology and a single delay path, 41 GHz mmW signal with 3 Gbps OOK NRZ data modulation was generated and delayed.

Index Terms—Microwave photonics, photonic integrated circuits, true time delays, optical ring resonators, millimeter wave communication, phased arrays.

I. INTRODUCTION

THE exponential mobile data usage growth is a major challenge for the current wireless communication network, and monthly data usage is expected to explode from 90 petabytes to 3.6 exabytes [1]. The 5th generation (5G) of mobile networks, which is assumed to deploy by 2020, will support enhanced coverage and increased bandwidth [2], [3]. It is believed that millimeter-wave (mmW) technology, with frequencies ranging from 30 GHz to 300 GHz, is a promising and cost-effective

candidate for 5G back-haul [4], [5]. For such high frequencies, traditional electronic RF driving methods and mmW signal propagation in coaxial cables are very inefficient [6]. Meanwhile, the highly directional nature of mmWs requires broadband phased array beam steering techniques. The basic electronic techniques using RF phase shifters causes undesirable beam squint across different frequencies, which limits the bandwidth. However, true time delay (TTD) avoids beam squint and steers the entire signal spectrum by the same angle [7]. An ideal alternate for the conventional electronic solutions is microwave photonics (MWP), taking advantage of the ultra-low-loss optical propagation and merging high-speed and high-responsivity uni-traveling-carrier photodiodes. MWP is advantageous in terms of changing the microwave frequencies and seamless integration with fiber optic networks [8]. The large bandwidth makes it suitable for realizing broadband optical TTDs [9], [10] and offering broadband optical beamforming networks (OBFNs).

Integrated photonics technology is an effective approach to address concerns of cost, size, weight and power consumption (CSWaP) of the devices [11], and is particularly advantageous for the realization of tunable optical TTDs allowing for precise path length control and feeding large scale phased array antennas (PAAs). It is also possible to integrate the OBFN with other optical components such as optical filtering [12], light sources, detectors, and modulators. Many different low-loss waveguide technologies have been proposed for the realization of integrated optical delay lines, as shown in Table I. The silicon on insulator (SOI) platform can realize waveguides in nano-scale that provides very compact footprint and high free spectral range [13]. However, the strong field confinement enhances loss induced by the sidewall roughness [14], and leads to non-linear effects which limit the maximum power [15]. Although the propagation loss can be reduced by using micron-scale waveguides, this trades the compact footprint and needs careful design to minimize higher-order mode excitation [16]. The indium phosphide (InP) platform is greatly advantageous in monolithic integration of active components such as lasers, detectors and modulators. Instead of only using heaters to tune the optical phase, plasmonic dispersion-based carrier injection tuning mechanisms are available in InP, which allows for high-speed low-power tunings. However, the loss of InP waveguides is relatively high with 1 dB/cm in undoped regions and 2 dB/cm in active regions [17]. Silicon nitride (Si_3N_4) with silicon oxide (SiO_2) cladding provides ultra-low-loss waveguide and have demonstrated

TABLE I
LOW-LOSS WAVEGUIDE TECHNOLOGIES FOR TTD

Platform	loss (dB/cm)	Tuning Mechanism	Active Integration	References
SOI	3 (nanowire) 0.35 (multimode)	Thermo-Optic (metal or doped Si heaters)	Hybrid on lasers, monolithic on modulators and Ge detectors	[13], [16], [28]
InP	1(undoped)/2(doped)	Thermo-Optic, Plasmonic Dispersion	Monolithic on all active components	[34]
Si_3N_4	0.1	Thermo-Optic	Hybrid on all active components	[23], [27], [29], [31]

propagation loss below 0.1 dB/cm. This platform can reduce the overall optical loss while consuming approximately an order of magnitude larger footprint than required for comparable structures in submicron SOI. These waveguides also demonstrate very high optical power handling up to 1-Watt in [18], which makes it possible to eliminate low noise amplifiers before antennas when doing microwave generation.

Integrated tunable optical delay lines are the key elements for optical beamforming networks (OBFNs). Thus far, several schemes have been implemented. The first is based on highly dispersive devices such as photonic crystal waveguides, which modifies the group index and dispersion by carefully designing a lattice structure as the waveguide cladding [19]–[22]. The second is realized by switching between delay lines with various lengths [16], [23]. This requires relatively simple control, but only supports discrete delays and the delay resolution is limited by the shortest delay line [6]. Another scheme uses all-pass filters such as optical ring resonators (ORRs), and is more powerful due to the small chip footprint and the ability to continuously tune the delay. However, the delay-bandwidth product for a single ORR is fixed [24]–[26]. The product could be increased by cascading multiple ORRs, which can be configured in coupled resonator optical waveguides (CROWs) [15], [27], [28] or side-coupled integrated spaced sequence of resonators (SCISSORs) [12], [13], [29], [30]. Although both CROW and SCISSOR delay elements theoretically allow for larger spectral bandwidth, SCISSOR delay elements shows more tolerance to manufacturing variation than CROW delay elements [11], [13]. Recently, researchers have successfully demonstrated OBFNs targeting Ku-band PAAs based on ORRs with SCISSOR structure [31]–[33].

In this work, based on multi-ORR SCISSOR structure and ultra-low-loss silicon nitride platform, we present 3-ORR based integrated 1×4 OBFNs with different sharing topologies targeting mmWs, with theoretical and experimental optimization of multi-ORR TTD. A mmW generation experiment was performed as well. For the remainder of the paper, ORR delay operating principles and the theoretically-optimized and quantitatively-studied for multi-ORR delays are discussed in Section II and III. Section IV discusses the device design and the testing stage of the fabricated chip. The experiments and results of multi-ORR TTD optimization and mmW generation discussed in Section V.

II. ORR DELAY OPERATING PRINCIPLES

A single ORR exhibits a bell-shaped group delay response, as depicted in Fig. 1(a), with the delay peak centered at the resonance frequency (f_r), and delay minima at the anti-resonant frequencies (f_{ar}), Targeting the ultra-low loss platform, a simple
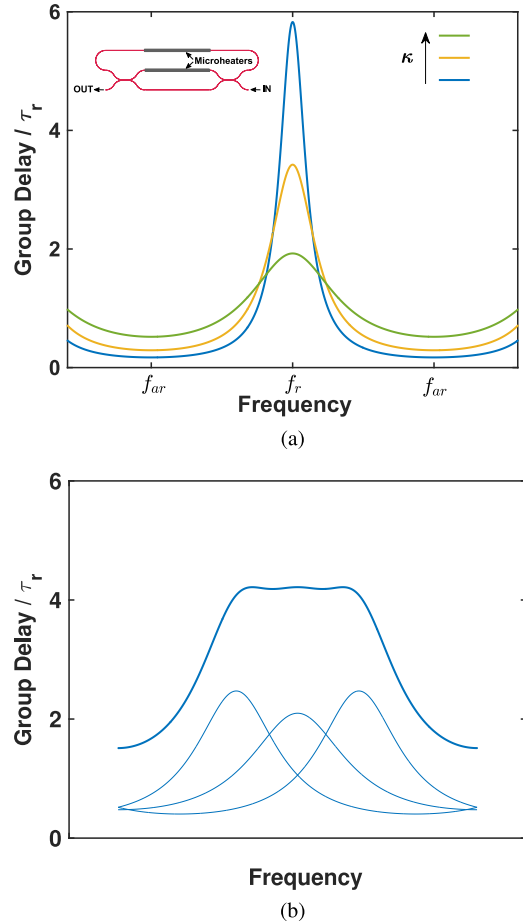

Fig. 1. (a) Single ORR bell-shaped group delay spectra for different values of κ. (b) Three cascaded ORR flattened delay response. f_r and f_{ar} refer to resonance frequency and anti-resonance frequency; τ_r refers to the round-trip propagation delay of the ring.

analytic expression for group delay of a single-ring ORR is given by

$$\tau_g(f) = \frac{\kappa \cdot \tau_r}{2 - \kappa - 2\sqrt{1-\kappa} \cdot \cos\left(2\pi \frac{f}{f_{FSR}} + \phi\right)} \quad (1)$$

where the free spectral range (f_{FSR}) and the round-trip propagation time (τ_r) are determined by the dimension of the ORR. ϕ and κ are the phase offset from the ring resonance and the power coupling coefficient, which determines the resonance frequency of the ORR and the shape of the curve, respectively. Due to the constant bandwidth-delay product, with increasing κ, the maximum group delay at f_r decreases rapidly whereas the minimum group delay at f_{ar} increases gradually, as shown in the Fig. 1(a). The group delay spectrum flattens, the bandwidth
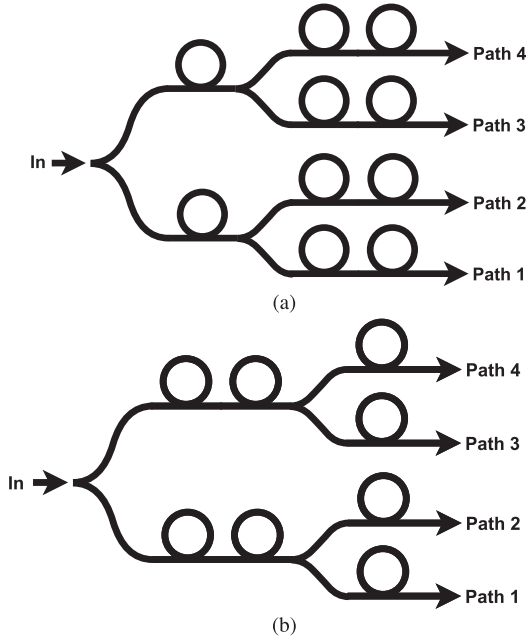
Fig. 2. Two-stage binary tree topologies for a 1×4 3-ORR-based OBFN with (a) one ring shared and (b) two rings shared.

increases accordingly. An inherent trade-off exists between the delay bandwidth and peak delay value.

Sufficient bandwidth and delays are both desired for wide bandwidth large-scale PAA applications. However, these quantities are constrained by the constant bandwidth-delay product of a single ORR. Cascading multiple ORRs can increase the product, and a flat group delay response with large bandwidth and delays can be achieved simultaneously if the coupling coefficient and phase shifter of each ORR are properly tuned, as illustrated in Fig. 1(b). The flattened group delay response, however, will yield delay ripple, or deviation from the desired delay across frequency. This ripple may distort the output microwave signal and possibly lead to system operation failure. The ripple can be reduced by cascading more rings, but this increases complexity of the photonic subsystem and the control.

Multi-ORR delay lines can form OBFNs with various topologies, which can provide different system complexities and delay ripples. Fig. 2 shows two stage binary tree topologies for a 1×4 3-ORR-based OBFN. The topology shown in Fig. 2(b) has two rings shared in the common stage, which has the minimum number of rings and delay response controls, whereas in the Fig. 2(a), the topology increases the number of rings and controls, and can has a more flattened delay response. Ultimately, for ORR-based time delays, inherent tradeoffs exist between bandwidth, ripple, delay, topology and complexity (number of rings). A detailed quantitative analysis of these tradeoffs and delay ripple optimizations will be discussed in Section III.

In the analysis, we neglect the loss of the ring waveguides thereby assuming all of the optical power at all frequencies will traverse the ORR without incurring loss. This is a good approximation for an ultra-low-loss waveguide platform. An ultra-low-loss waveguide is necessary for a ORR based OBFN. In the under-coupling regime, superluminal and negative group velocity phenomena [35] will be exhibited around the resonance

frequency and consequently limit the maximum delay of the ORR. A low waveguide loss will give a small critical coupling (κ_c) and thus a large achievable delay. Moreover, for a mmW beamforming system, the RF signal power is proportional to the square of the input light intensity and is more sensitive to the optical loss. This would impact the OBFN scalability. In addition, a low waveguide loss could also improve the power uniformity for an antenna array.

III. THEORETICAL OPTIMIZATION FOR MULTI-ORR DELAYS

To evaluate the inherent tradeoffs of multi-ORR based delays, we utilized the lossless ORR delay model (1) and applied a standard genetic algorithm to minimize the delay ripple. The genetic algorithm is a global optimization algorithm for nonlinear problems. In this study, we normalized the group delay, delay ripple and bandwidth to round trip delay τ_r and ring free spectrum range (FSR) to make the analysis applicable to generic ORRs. The cost function, which also defines the normalized ripple, was chosen as the maximum delay deviation from the target value within the desired bandwidth, which can be expressed as

$$\mathbf{R}(f) = \max \left\{ \frac{|\tau_g(f) - \tau_{g0}|}{\tau_r}, \ f \in \text{desired bandwidth} \right\} \quad (2)$$

Since a genetic algorithm has the probability of being trapped in a local optimal solution, the algorithm was repeated more than 50 times to ensure a global optima.

Fig. 3(a) shows the relation between ripple and bandwidth for various target group delays for a single 3-ORR delay line. For the delay range of $\tau_g > 3\tau_r$ (blue curves), the group delay response is flattened with the resonance frequency of the three bell-shaped group delay spectrum of the single-ORR delay elements, where the ripple is smaller for smaller target delay (larger κ). In the range $\tau_r < \tau_g < 3\tau_r$ (red and green curves), the group delay response is flattened by the delay curves of two rings at the anti-resonance and the delay at the resonance of the other ring with large κ. The last region, $\tau_g < \tau_r$ (black curves) only two rings are utilized for flattening the group delay response, hence the ripple is relatively large for large bandwidth and small ripple. The ripple of 5-ORR element was also characterized and the results are shown in Fig. 3(b). As expected, adding two more rings improves the bandwidth significantly. For a dynamic tuning range of $2\tau_r$ and ripple smaller than 0.01, a 5-ORR delay can achieve a bandwidth up to 0.5, while for 3-ORR delay, the bandwidth is 0.25, which corresponds to bandwidths of 11.5 GHz and 5.75 GHz for ORRs with FSR = 23 GHz, respectively. Table II shows a typical loop-up table for an optimized 3-ORR delay line with a normalized TTD bandwidth of 0.275.

Although increasing the number of rings improves performance, this also increases the system complexity considerably. To limit the total number of rings, adjacent paths can be made to share one or more rings. However, sharing of rings impacts the ability to minimize ripple since the delay response of each path has to compromise with its neighbor path to achieve a joint ripple minimization. We investigate this further by studying the effect two topologies depicted in Fig. 2 on ripple minimization. The relations between ripple, bandwidth, and target group delays for a 3-ORR delay line with one shared ring and with two
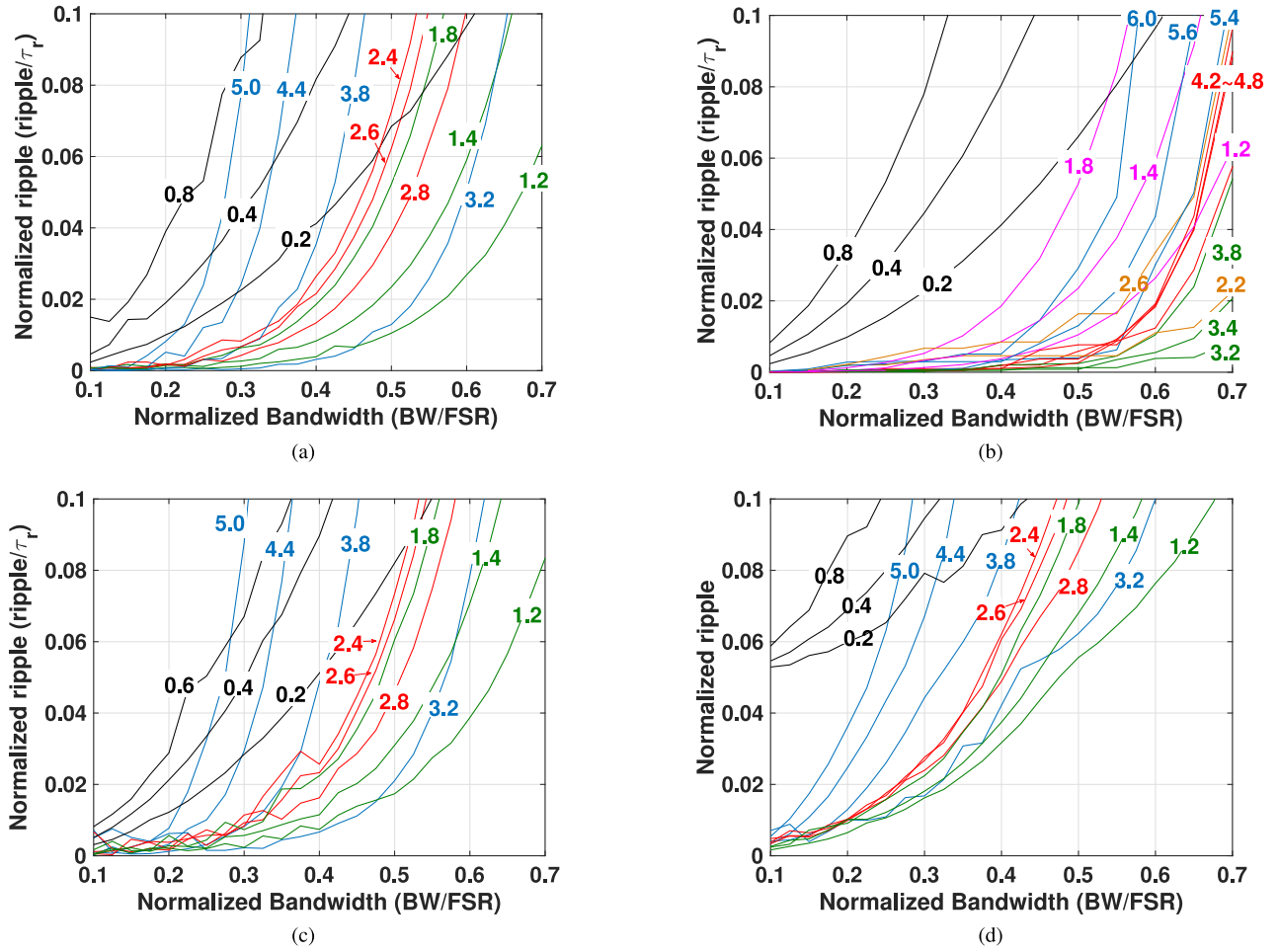
Fig. 3. Ripple for (a) 3-ORR and (b) 5-ORR delay lines for various target delays. Ripple for (c) 3-ORR with one shared ring and (d) 3-ORR with two shared rings for various target delays.

TABLE II
TYPICAL LOOK-UP TABLE FOR OPTIMIZED 3-ORR DELAY LINE WITH A
NORMALIZED TTD BANDWIDTH OF 0.275

Normalized Delay	κ_1	$\kappa_{2/3}$	$\phi_2/-\phi_3$(rad)
4.8	0.8154	0.7539	0.9249
4.2	0.8803	0.8261	1.0618
3.8	0.9269	0.8821	1.1806
3.4	0.9642	0.9359	1.3808
3.2	0.9792	0.9624	1.5590
2.6	0.9815	0.9490	2.8025
2.2	0.9752	0.8001	2.5066
1.8	0.9867	0.6588	2.7576
1.6	0.9891	0.4912	2.5032
0.6	0	0.6705	2.9489
0.2	0	0.3035	3.0273

κ_x and ϕ_x refer to the coupling coefficient and phase offset from the resonance of ring$_x$, as described in (1), ϕ_1 is set to zero in the simulation.

shared rings are shown in Fig. 3(c) and (d), respectively. Compared to the 3-ORR delay line with no shared rings [Fig. 3(a)], we can conclude that sharing two rings has the least complexity but likely limits the bandwidth, whereas sharing one ring for two adjacent paths could reduce the number of rings without significantly limiting the performance.

IV. DEVICE DESIGN AND TESTING STAGE

Two topologies of ORR based 1×4 OBFN chips are shown in Fig. 2. The chips have a footprint of 8×32 mm^2 and the architecture is similar to that reported in [19]. The OBFN chips were realized for C-band operation and fabricated with an ultra low-loss silicon nitride waveguide technology demonstrating low optical loss less than 0.1 dB/cm [36]. The architecture of the ring resonator is shown in Fig. 4(a). Symmetric Mach-Zehnder interferometers (MZIs) are employed as the tunable coupler from the bus waveguide to the ring. A chromium heater is incorporated to thermally and continuously tune the coupling coefficient over range of 0 to 1. Another chromium heater is also designed on top of the ring waveguide to thermally tune the ring resonant frequency. The ORRs are designed to have a FSR of 22 GHz. An IR image of an operating ORR with small κ is shown in Fig. 4(a) showing strong scattering since very high optical power is trapped in the ring. At both edges of the chip, two waveguide arrays are included with a pitch of 127 μm so that the chip can be pigtailed to a standard commercial fiber array for optical input and output. These waveguides are tapered to match the mode size of the fiber array in order to improve the coupling efficiency.
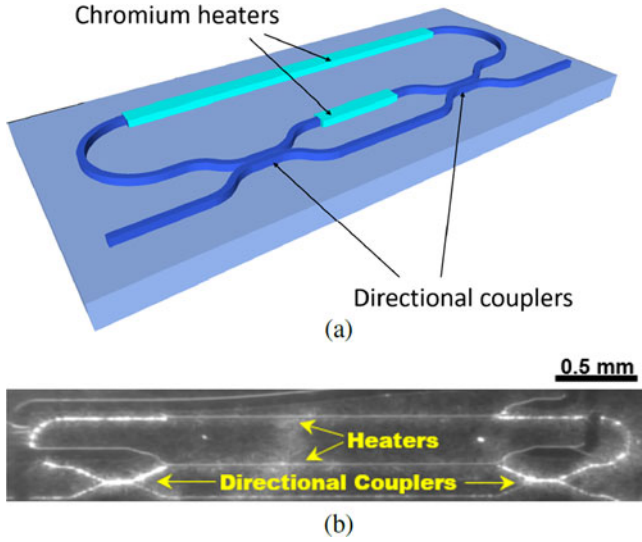
Fig. 4. (a) Sketch of the ORR-based delay element. (b) IR image of the ORR under operation. The bright traces indicate the waveguides with light propagation, whereas the dark traces indicate heaters and metal traces.
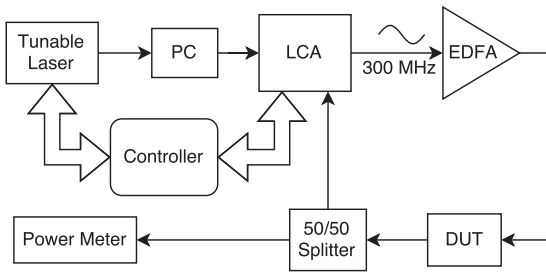

Fig. 5. Group delay response characterization setup. (PC: polarization controller; LCA: lightwave component analyzer; DUT: device under test; EDFA: erbium-doped fiber amplifier.)
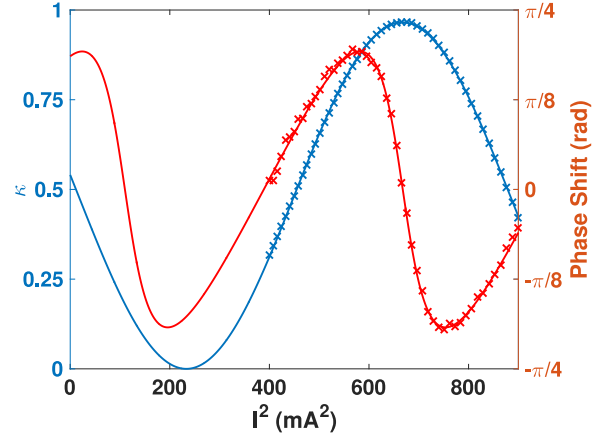

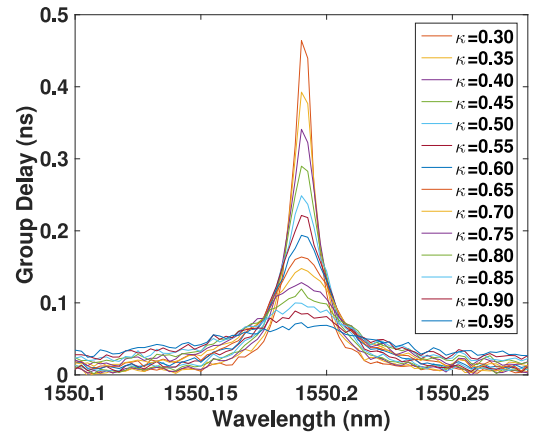Fig. 6. Coupling coefficient (blue) and induced ring round-trip phase shift (red) of the ORR MZI coupler.

Fig. 7. Calibrated single ORR delay spectra for a given central wavelength and various coupling coefficients.

The fabricated chip is mounted on a copper stage and the temperature is stabilized with a thermoelectric cooler. Two standard commercial fiber arrays are attached to the edge of the optical coupling. The metal leads of phase shifters on the chip are routed to the long edges and connect with a customized 40-pin DC probe. The OBFN, as shown in Fig. 2, has at least 16 phase shifters that need to be controlled individually. Given such a number of phase shifters and the scalability of the OBFN, we developed a scalable, compact and programmable multi-channel controller to provide full control to the chip. The fiber to chip coupling loss was measured to be 5 dB/facet and the heater tuning efficiency was measured to be 5.3π rad/W.

V. EXPERIMENTS AND DISCUSSION

A. Single-ORR Delay Calibration

The group delay response of the OBFN chip can be characterized using a standard modulation phase shift method, as shown in Fig. 5. A C-band laser is modulated by a lightwave component analyzer (LCA) with a 300 MHz sinusoidal RF signal. The light is coupled to the chip after amplification by an erbium-doped fiber amplifier (EDFA), and then returned to the LCA. By measuring the RF phase shift $\Delta\phi$ of the signal, the group delay can be expressed as:

$$\tau_g(\lambda) = \frac{\Delta\phi(\lambda)}{2\pi f_0} \tag{3}$$

where λ is the wavelength, $\Delta\phi$ is the measured phase shift and f_0 is the modulation frequency. In addition to the delay of OBFN on the chip, the delays of the waveguides and fibers are also included in the measurement, which are eliminated by fitting the measured delay response with a lossless ring resonator delay response model (1) with a constant delay term representing the additional delays.

Since a symmetric MZI coupler is used for the ring resonator, it will induce a variable phase shift for light passing the MZI coupler, which can be interpreted as a shift in the ring delay response as we tune the coupling coefficient. This phase shift can be studied utilizing transfer matrix techniques given by

$$T = \begin{bmatrix} T_{11} & T_{12} \\ T_{21} & T_{22} \end{bmatrix} \tag{4}$$

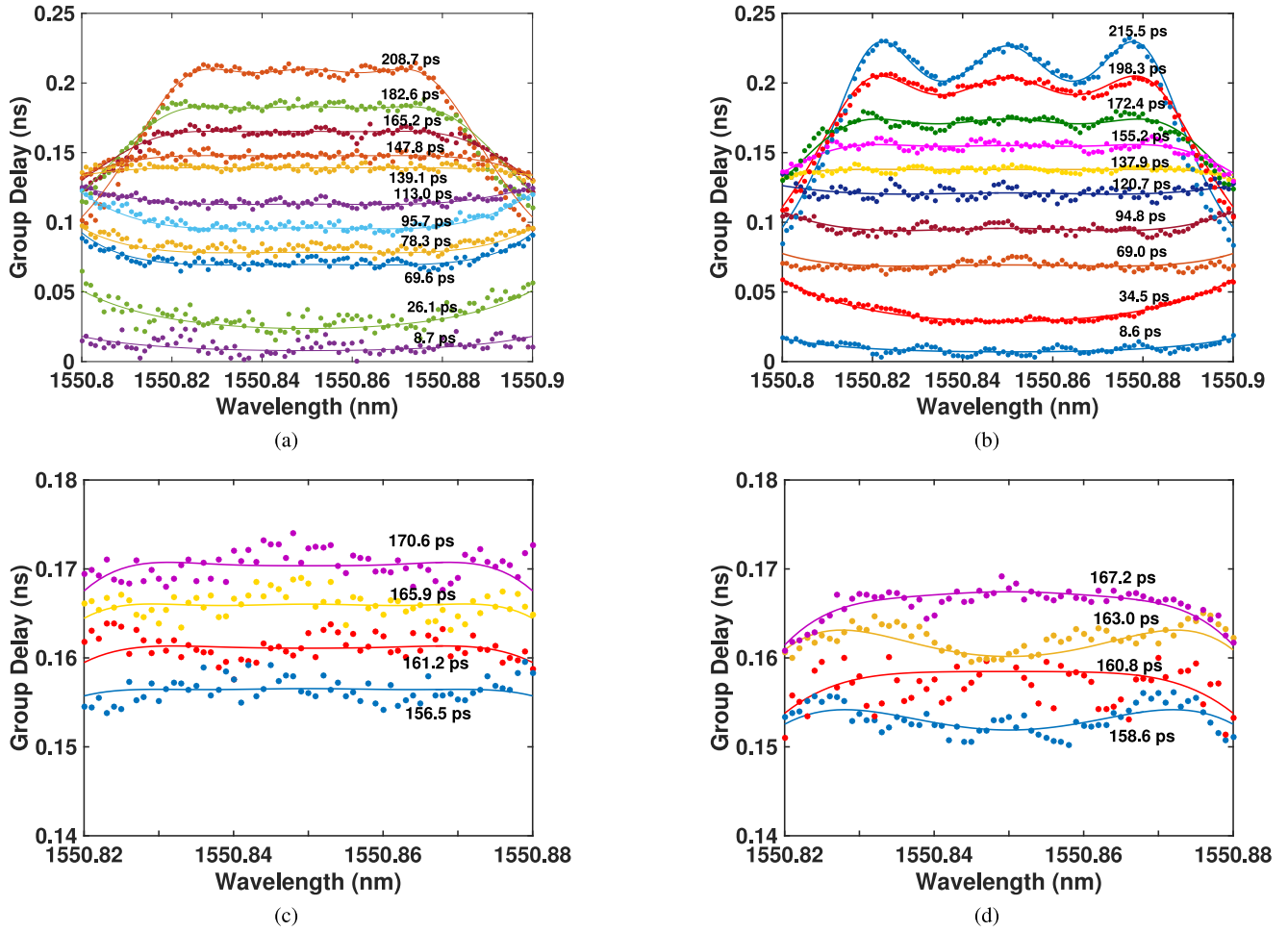$$T_{11} = (1 - \kappa)e^{-j\Delta\psi} - \kappa \tag{5}$$

Fig. 8. Ripple optimized group delay spectra for 3-ORR delay line with (a) no ring shared, (c) one shared ring, and (d) two shared rings at the TTD bandwidth of 6.3 GHz, and (b) no ring shared at the bandwidth of 8.6 GHz. The dots denote the measured delays, whereas the solid curves denote the simulation result.

$$T_{12} = T_{21} = 2\sqrt{\kappa(1-\kappa)} \cos \frac{\Delta\psi}{2} e^{-j\left(\frac{\Delta\psi}{2} + \frac{\pi}{2}\right)} \qquad (6)$$

$$T_{22} = (1-\kappa) - \kappa e^{-j\Delta\psi} \qquad (7)$$

where κ is the coupling coefficient of directional coupler in the MZI, and $\Delta\psi$ is the phase difference between two MZI arms, which is proportional to the square of heater current. By sweeping the heater current of the coupler, and fit the data using (1), (5), (6), the relation between the coupling, phase shift of the MZI coupler and tuning current can be given by Fig. 6. The FSR of the ORR was measured to be 23.1 GHz, which is close to the designed FSR. Using this relation, we can compensate the undesired phase shift and set the resonance frequency of the ORR accurately. A verification test showing group delay spectra for various coupling coefficients with a given resonant frequency is given in Fig. 6, which demonstrates an accurate calibration and controllability for tuning the group delay of a single ORR.

B. Multi-ORR Delay Optimization

For OBFNs targeting mmW, a high-quality TTD response is required to avoid beam squint, which is one of the dominant issue limiting the high bit rate data transmission. Multi-ORRs can provide a large delay-bandwidth product yielding a large delay and bandwidth simultaneously, but this requires a optimized tuning of coupling and resonance of each ORR in the OBFN. We first optimized the coupling coefficients and resonance frequencies of all the rings in the multi-ORR delay line using the optimization result in Section III, and then generated the theoretical delay response as a reference to tune the rings. A realtime delay response measurement system was developed to help with this tuning. After applying the calibration to every ORR in the OBFN, the resonance frequency and coupling coefficient of each ORR was set based on the individual optimization result. However, the OBFN exhibited a thermal crosstalk that reduces the tuning accuracy when attempting to simultaneously tune all the ORRs in a delay path. Therefore, in addition to using the optimized data set, we manually tuned the ORRs to compensate the offset induced by the thermal cross talk. Fig. 8(a) shows the optimized delay response of a single 3-ORR delay line and demonstrates a bandwidth of 6.3 GHz. The ripple is more evident at higher delays. Without any noticeable ripple, a dynamic tuning range of 208.7 ps was achieved, which corresponds to a phase shift of 17.1π for a 41 GHz W-band signal. According to our previous work, the delay line has a maximum loss of 3.3 dB
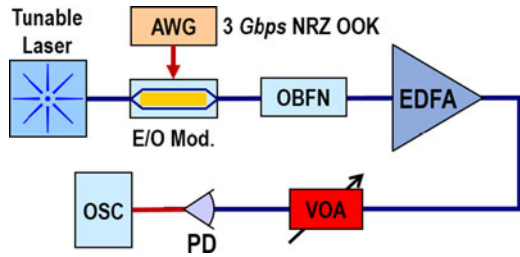
Fig. 9. Data transmission test setup for single 3-ORR true time delay lines. (OSC: oscilloscope; Mod.: modulator; AWG: arbitrary waveform generator; VOA: variable optical attenuator; PD: photodiode.)

for the delay of 208.7 ps [37]. A delay response for a bandwidth of 8.6 GHz, shown in Fig. 8(b), was also achieved. However, the ripple at high delay is more noticeable, and the dynamic tuning range falls to 172.4 ps and phase shift of 14.1π, which exhibits the tradeoffs between the bandwidth, delay and ripple for a multi-ORR delay line as discussed in Section III.

Fig. 8(c) and (d) show the optimized delay response of all the four paths of the OBFN for the topologies of with one shared ring and two shared rings with a TTD bandwidth of 6.3 GHz, as shown in in Fig. 2(a) and (b), respectively. Each path was tuned to have ~4.6 ps more delay than its previous path, which is equivalent to a 22° of beamsteering angle for a 41 GHz half-wavelength dipole antenna array. Comparing Fig. 8(c) and (d), we can see that the topology sharing two rings [Fig. 2(b)] yields a ripple around 1.5 ps, whereas the topology sharing one ring [Fig. 2(a)] provides a inperceptible ripple. Therefore, for a 3-ORR based OBFN, the topology sharing one ring in the common path can maintain a small ripple in the delay response while maintaining a moderate system complexity, which is a promising path for wideband applications.

C. Data Transmission Delay Experiment

A systematic test of the 3-ORR delay line using the setup in Fig. 9 was performed to evaluate the 3-ORR delay overall performance. An external cavity laser (ECL) is modulated with a 3 Gbps OOK NRZ data signal by a Mach-Zehnder modulator (MZM) driven by an arbitrary waveform generator (AWG), and then sent into a OBFN chip optimized to various delays with the bandwidth of 8.6 GHz. The output of the chip was amplified by an EDFA, and detected and monitored by a photodiode and an oscilloscope. Fig. 10 shows the eye-diagram after the 3-ORR tunable true time delay line over the delay range of 0–209 ps, where open and clear eyes are preserved. The delay of the transmitted signal can be continuously tuned up to 209 ps, which is consistent with the delay response characterizations shown in Fig. 8(a). In the desired working range (0–172.4 ps), no signal deterioration was observed, whereas for higher delays, small signal distortion was observed due to the increasing ripple (dispersion) in the delay response. This test confirms the accurate control and continuous tunability for the optimized 3-ORR delay line. The power consumption varies depending on the delays or the ring tuning parameters. Within the delay tuning range in this measurement, the total power consumption for the 3-ORR line varies from 1.25 W to 2.57 W, which is relatively
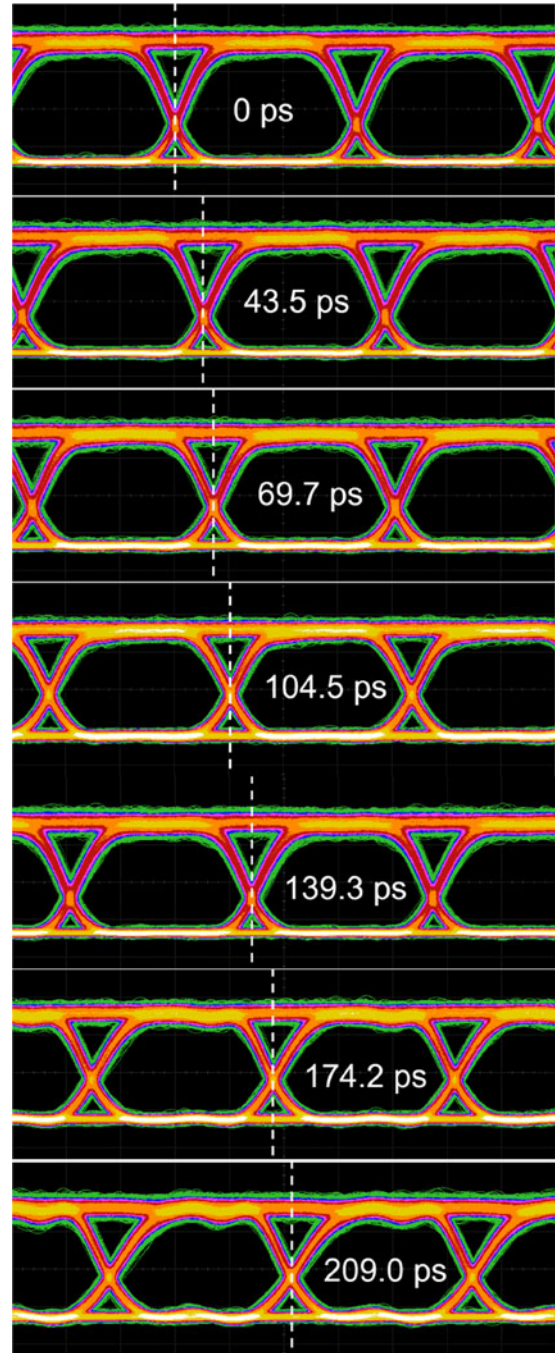
Fig. 10. Tunable 3-ORR true time delay line test with 3 Gbps OOK NRZ modulation for tuning range of 0 to 209 ps.

high since the silicon nitride platform has a low thermo-optical coefficient.

D. Millimeter Wave Generation and Distribution

A system test was performed for mmW generation through simultaneous frequency up-conversion heterodyne process with one path of the OBFN [38]. The schematic of the experimental setup is as depicted in Fig. 11(b). The coherent laser light is modulated by driving a null biased MZM modulator with a local oscillator (LO) of half the mmW carrier frequency,

Fig. 11.   mmW generation and delay experiment test setup. (ESA: electrical spectrum analyzer; OSA: optical spectrum analyzer; DE/MUX: de/multiplexer.)

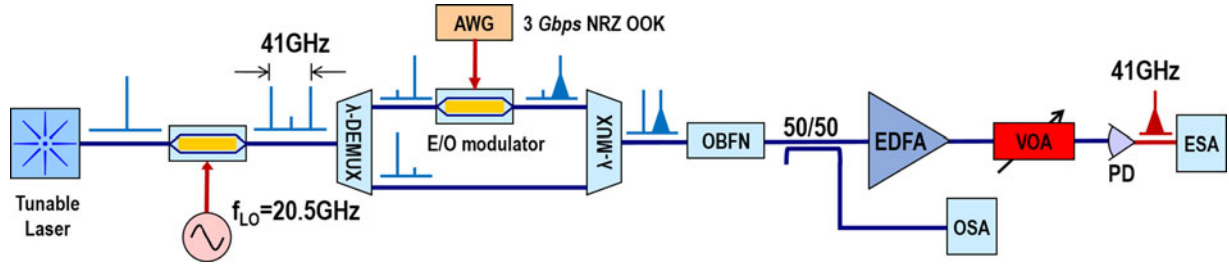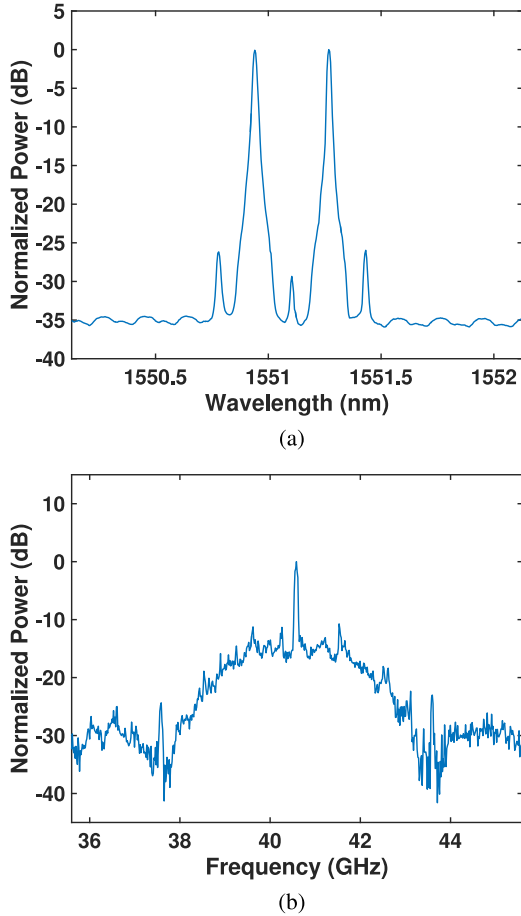Fig. 12.   (a) Normalized optical spectrum for one path of the chip outputs. (b) Normalized electrical spectrum at the photodiode with 3 Gbps OOK NRZ modulation.

which suppresses the central optical carrier but generates two dominant optical sidebands spaced by the mmW carrier frequency. A standard wavelength division multiplexing (WDM) with 50 GHz channel grids separates the two sidebands. One sideband is modulated by a quadrature biased MZM driven by an AWG and serves as the data tone, and the other sideband serves as the reference tone for the heterodyne process. The two optical tones are combined by another identical WDM and both tones are coupled to the OBFN chip. The signal is split into four paths and appropriately delayed depending on the desired beamsteering angle. The output signal of one path is then amplified by an EDFA. After properly attenuation, the two optical

sidebands heterodyne at a high speed photodiode to generate the data signal with mmW carrier. Polarization maintaining fibers are employed for all the optical connections, making the system simple and robust.

The laser wavelength, center wavelength of the delay line and the channel wavelengths of the WDMs need to be matched in the system. The wavelength of the laser is set to the middle between two WDM channels at 1551.10 nm. One path of the OBFN chip is used and optimized to have a delay of 157 ps and bandwidth of 8.6 GHz centered at the central wavelength of the data sideband. The preliminary test was done at mmW frequency of 41 GHz, where the LO should be set to 20.5 GHz. The output signal from the OBFN chip is tapped and monitored by an optical spectrum analyzer, which shows the two dominated sidebands centered at 1550.94 nm and 1551.27 nm, respectively, as depicted in Fig. 12(a). The AWG generates a 3 Gbps OOK NRZ signal, and optical power before the photodiode is 5 dBm. Fig. 12(b) provides the generated 41 GHz mmW signal spectrum with the data band, which is measured by an high speed electrical spectrum analyzer. The available data rate of the system is determined by the TTD bandwidth of the delay line. In our case, the bandwidth of the delay line is 8.6 GHz which can support a much higher data rate by employing more advanced modulation formats. In addition, the mmW frequency generated by the up-conversion process is widely tunable and can go up to double of the LO and the modulator bandwidth.

VI. CONCLUSION

In this work, we reported 3-ORR SCISSOR structure based integrated 1×4 OBFNs with different sharing topologies targeting a mmW PAA. The OBFN chip are fabricated on ultra-low loss silicon nitride platform. The group delay ripple of multi-ORR delay lines were theoretically optimized and quantitatively studied by applying a genetic algorithm, showing the tradeoffs among bandwidth, delay, ripple and different topologies. The optimized 3-ORR delay responses was experimentally achieved, which exhibits 208.7 ps and 172.4 ps of dynamic tuning range for TTD bandwidth of 6.3 GHz and 8.7 GHz, which corresponds to a phase shift of 17.1π and 14.1π for a 41 GHz mmW signal, respectively. The TTD performance of the 3-ORR delay line was also verified by control the delay of a 3 Gbps data stream. The optimized output of OBFN was achieved with 4.6 ps delay difference from its neighboring paths, which is equivalent to a $22°$ of beamsteering angle for a 41 GHz half-wavelength dipole antenna array. Both the theoretical analysis and experiment

exhibit that the topology with one ring shared could balance the system complexity and bandwidth well. A 41 GHz mmW signal was generated as well with 3 Gbps OOK NRZ data modulation and the frequency can be easily tuned to other bands such as W-band mmW.

REFERENCES

[1] M. Kavehrad, "Optical wireless applications: A solution to ease the wireless airwaves spectrum crunch," in *Proc. SPIE 8645, Broadband Access Commun. Technol. VII*, B. B. Dingel, R. Jain, and K. Tsukamoto, Eds. Jan. 2013, p. 86450G.

[2] V. Jungnickel *et al.*, "The role of small cells, coordinated multipoint, and massive MIMO in 5G," *IEEE Commun. Mag.*, vol. 52, no. 5, pp. 44–51, May 2014.

[3] C. Wang *et al.*, "Cellular architecture and key technologies for 5G wireless communication networks," *IEEE Commun. Mag.*, vol. 52, no. 2, pp. 122–130, Feb. 2014.

[4] M. J. R. Heck and H. Mohammadhosseini, "Energy-efficient millimeter-wave generation using silicon photonics," in *Proc. Silicon Photon. XII*, G. T. Reed and A. P. Knights, Eds. Feb. 2017, p. 101080O.

[5] W. Feng, Y. Li, D. Jin, L. Su, and S. Chen, "Millimetre-wave backhaul for 5G networks: Challenges and solutions," *Sensors*, vol. 16, no. 6, Jun. 2016, Art no. E892.

[6] S. Iezekiel, M. Burla, J. Klamkin, D. Marpaung, and J. Capmany, "RF engineering meets optoelectronics: Progress in integrated microwave photonics," *IEEE Microw. Mag.*, vol. 16, no. 8, pp. 28–45, Sep. 2015.

[7] I. Frigyes and A. J. Seeds, "Optically generated true-time delay in phased-array antennas," *IEEE Trans. Microw. Theory Tech.*, vol. 43, no. 9, pp. 2378–2386, Sep. 1995.

[8] X. Pang *et al.*, "100 Gbit/s hybrid optical fiber-wireless link in the W-band (75–110 GHz)," *Opt. Express*, vol. 19, no. 25, p. 24944, Dec. 2011.

[9] Y. Liu *et al.*, "Ring resonator true time delay arrays with sharing optimization for wideband applications," in *Proc. Adv. Photon. (IPR, NOMA, Sensors, Networks, SPPCom, PS), Pap. IW2A.2*, Jul. 2017, p. IW2A.2.

[10] J. Capmany and D. Novak, "Microwave photonics combines two worlds," *Nat. Photon.*, vol. 1, no. 6, pp. 319–330, Jun. 2007.

[11] J. A. Nanzer, A. Wichman, J. Klamkin, T. P. McKenna, and T. R. Clark, "Millimeter-wave photonics for communications and phased arrays," *Fiber Integr. Opt.*, vol. 34, no. 4, pp. 159–174, Jul. 2015.

[12] L. Zhuang *et al.*, "Novel low-loss waveguide delay lines using Vernier ring resonators for on-chip multi-λ microwave photonic signal processors," *Laser Photon. Rev.*, vol. 7, no. 6, pp. 994–1002, Nov. 2013.

[13] J. Xie, *et al.*, "Continuously tunable reflective-type optical delay lines using microring resonators," *Opt. Express*, vol. 22, no. 1, p. 817, Jan. 2014.

[14] W. Bogaerts *et al.*, "Silicon microring resonators," *Laser Photon. Rev.*, vol. 6, no. 1, pp. 47–73, 2012.

[15] F. Morichetti, A. Melloni, C. Ferrari, and M. Martinelli, "Error-free continuously-tunable delay at 10 Gbit/s in a reconfigurable on-chip delay-line," *Opt. Express*, vol. 16, no. 12, p. 8395, Jun. 2008.

[16] X. Wang *et al.*, "Continuously tunable ultra-thin silicon waveguide optical delay line," *Optica*, vol. 4, no. 5, p. 507, May 2017.

[17] M. Smit *et al.*, "An introduction to InP-based generic integration technology," *Semicond. Sci. Technol.*, vol. 29, no. 8, Jun. 2014, Art no. 083001.

[18] C. G. H. Roeloffzen *et al.*, "Silicon nitride microwave photonic circuits," *Opt. Express*, vol. 21, no. 19, Sep. 2013, Art no. 22937.

[19] H. Schippers *et al.*, "Broadband conformal phased array with optical beam forming for airborne satellite communication," in *Proc. IEEE Aerosp. Conf.*, IEEE, Mar. 2008, pp. 1–17.

[20] C.-Y. Lin *et al.*, "Silicon nanomembrane based photonic crystal waveguide array for wavelength-tunable true-time-delay lines," *Appl. Phys. Lett.*, vol. 101, no. 5, Jul. 2012, Art no. 051101.

[21] J. Sancho *et al.*, "Integrable microwave filter based on a photonic crystal delay line," *Nat. Commun.*, vol. 3, no. 1, Jan. 2012, Art no. 1075.

[22] N. Ishikura *et al.*, "Photonic crystal tunable slow light device integrated with multi-heaters," *Appl. Phys. Lett.*, vol. 100, no. 22, May 2012, Art no. 221110.

[23] R. L. Moreira *et al.*, "Integrated ultra-low-loss 4-Bit tunable delay for broadband phased array antenna applications," *IEEE Photon. Technol. Lett.*, vol. 25, no. 12, pp. 1165–1168, Jun. 2013.

[24] G. Lenz, B. Eggleton, C. Madsen, and R. Slusher, "Optical delay lines based on optical filters," *IEEE J. Quantum Electron.*, vol. 37, no. 4, pp. 525–532, Apr. 2001.

[25] L. Yosef Mario and M. K. Chin, "Optical buffer with higher delay-bandwidth product in a two-ring system," *Opt. Express*, vol. 16, no. 3, Feb. 2008, Art no. 1796.

[26] Y. Liu *et al.*, "Ring resonator delay elements for integrated optical beam-forming networks: Group delay ripple analysis," in *Proc. Adv. Photon. (IPR, NOMA, Sensors, Networks, SPPCom, SOF)*, 2016, p. IW1B.3.

[27] F. Morichetti *et al.*, "A reconfigurable architecture for continuously variable optical slow-wave delay lines." *Opt. Express*, vol. 15, no. 25, pp. 17 273–82, Dec. 2007.

[28] M. L. Cooper *et al.*, "Waveguide dispersion effects in silicon-on-insulator coupled-resonator optical waveguides," *Opt. Lett.*, vol. 35, no. 18, Sep. 2010, Art no. 3030.

[29] Y. Liu *et al.*, "Single ring resonator delays for integrated optical beam forming networks," in *Proc. IEEE Int. Topical Meeting Microw. Photon.*, vol. 7, 2016, pp. 321–324.

[30] Y. Liu *et al.*, "Ring resonator based integrated optical beam forming network with true time delay for mmW communications," in *Proc. IEEE MTT-S Int. Microw. Symp.*, IEEE, Jun. 2017, pp. 443–446.

[31] L. Zhuang *et al.*, "Novel ring resonator-based integrated photonic beam-former for broadband phased array receive antennas—Part II: Experimental prototype," *J. Lightw. Technol.*, vol. 28, no. 1, pp. 19–31, Jan. 2010.

[32] C. Roeloffzen, P. van Dijk, D. Marpaung, M. Burla, and L. Zhuang, "Development of a broadband integrated optical beamformer for Kuband phased array antennas." in *Proc. 34th ESA Antenna Workshop*, 2012, pp. 3–5.

[33] N. M. Tessema *et al.*, "Wavelength-dependent continuous delay based on a Si_3N_4 optical ring resonator for K-band radio beamformer," in *Proc. IEEE Int. Topical Meeting Microw. Photon.*, 2016, pp. 305–308.

[34] D. Melati, A. Waqas, Z. Mushtaq, and A. Melloni, "Wideband integrated optical delay line based on a continuously tunable Mach–Zehnder interferometer," *IEEE J. Sel. Topics Quantum Electron.*, vol. 24, no. 1, pp. 1–8, Jan. 2018.

[35] H. P. Uranus and H. J. W. M. Hoekstra, "Modeling of loss-induced super-luminal and negative group velocity in two-port ring-resonator circuits," *J. Lightw. Technol.*, vol. 25, no. 9, pp. 2376–2384, Sep. 2007.

[36] R. G. Heideman, A. Leinse, M. Hoekman, F. Schreuder, and F. H. Falke, "TriPleX™: The low loss passive photonics platform: Industrial applications through multi project wafer runs," in *Proc. IEEE Photon. Conf.*, IEEE, Dec. 2014, pp. 224–225.

[37] Y. Liu *et al.*, "Tuning optimization of ring resonator delays for integrated optical beam forming networks," *J. Lightw. Technol.*, vol. 35, no. 22, pp. 4954–4960, Nov. 2017.

[38] T. P. McKenna, J. A. Nanzer, and T. R. Clark, "Experimental demonstration of photonic millimeter-wave system for high capacity point-to-point wireless communications," *J. Lightw. Technol.*, vol. 32, no. 20, pp. 3588–3594, Oct. 2014.

Yuan Liu received the B.S. degree from Harbin Institute of Technology, Harbin, Heilongjiang Sheng, China, the M.S. degree in condensed matter physics from the Technical Institute of Physics and Chemistry, Chinese Academy of Sciences, Beijing, China, and the another M.S. degree in electrical and computer engineering from the University of California Santa Barbara (UCSB), Santa Barbara, CA, USA, in 2009, 2012, and 2014, respectively. He is currently working toward the Ph.D. degree at the UCSB with emphasis on photonic integrated circuits and microwave photonics.

Adam R. Wichman received the B.S. degree in electrical engineering with distinction from the United States Naval Academy, Annapolis, MD, USA, in 1992 and the Ph.D. degree in electrical engineering from Brown University, Providence, RI, USA, in 2018, where he was a National Defense Science and Engineering Graduate Fellow. He is currently a Member of the technical staff with MIT Lincoln Laboratory, Lexington, MA, USA.

Brandon Isaac received the B.S. degree in physics and chemical engineering from the University of Kentucky, Lexington, KY, USA, in 2013. He has also received the Ph.D. degree from the University of California Santa Barbara (UCSB), Santa Barbara, CA, USA, working on molecular beam epitaxy for fundamental materials research for the first 2 years. He is currently working on the high performance optoelectronic devices and photonic-integrated circuits for phased arrays applications.

Jean Kalkavage received the M.S. degree in electrical engineering from Boston University, Boston, MA, USA, in 2014. She is currently with the Johns Hopkins University Applied Physics Laboratory, Laurel, MD, USA. Her experience is concentrated in the technology areas of microwave photonics, digital communications, and photonic integrated circuits. She is an active member of the IEEE Photonics Society.

Eric J. Adles (SM'15) received the B.S. and Ph.D. degrees in physics from North Carolina State University, Raleigh, NC, USA, in 1994 and 2007, respectively. His graduate research focused on the application of second-harmonic generation for real-time optical diagnostics of semiconductors. From 2009 to 2010, he was a Postdoctoral Researcher with the University of Maryland Baltimore County, Baltimore, MD, USA, where he worked on optoelectronic oscillators and photonic phase noise measurement systems. He is currently a member of the Principal Professional Staff with the Johns Hopkins University Applied Physics Laboratory, Laurel, MD, USA, working on photonic systems for radio frequency and digital communication applications. He is a member of the IEEE Photonics Society, the Optical Society of America, and the American Physical Society.

Thomas R. Clark, Jr. (M'99–SM'05) received the B.S. degree from Loyola College, Baltimore, MD, USA, the M.S. degree from Lehigh University, Bethlehem, PA, USA, and the Ph.D. degree from the University of Maryland, College Park, MD, USA, in 1991, 1993, and 1998, respectively, all in physics. He is currently a Supervisor of the Electro-Optical and Infrared Systems and Technologies Group and a member of the Principal Professional Staff with The Johns Hopkins University Applied Physics Laboratory, Laurel, MD, USA. From 1998 to 2000, he was a Research Physicist with the Optical Sciences Division, Naval Research Laboratory, Washington, DC, USA, where his research interests were in the fields of low-noise lasers and microwave photonics. In 2000, he joined the venture-backed Dorsal Networks, Columbia, MD, USA, later acquired by Corvis Corporation, Columbia, MD, USA, where he was a Senior Optical Design Engineer developing hardware and simulation tools for telecommunications applications, including undersea and terrestrial WDM transmission systems, optical amplifiers, optical transceivers, and system control modules. From 2003 to 2010, he was a member of the Senior Professional Staff (2003–2007) and Principal Professional Staff since 2007 with The Johns Hopkins University Applied Physics Laboratory. His research interests include the study of lasers and nonlinear optics, the development and characterization of low-noise and ultrafast photonic systems and devices, and the application of photonics to problems in optical communications and microwave and millimeter-wave systems. He is a member of OSA. He was the 2011 Chair of the OSA/IEEE Optical Fiber Communications subcommittee on Optical Processing and Analog Subsystems, the 2013 Co-Technical Program Chair for the IEEE Microwave Photonics Conference, and the Chair of the IEEE Photonics Conference subcommittee on Microwave Photonics from 2010 to 2012. He was Technical Program Chair/Member-at-Large/General Program Chair for the 2014/2015/2016 IEEE Photonics Conference.

Jonathan Klamkin (SM'14) received the B.S. degree from Cornell University, Ithaca, NY, USA, in 2002, and the M.S. and Ph.D. degrees from the University of California Santa Barbara, Santa Barbara, CA, USA, in 2004 and 2008, respectively. From 2008 to 2011, he was a Member of the Technical Staff with the Electro-Optical Materials and Devices Group, MIT Lincoln Laboratory. From 2011 to 2013, he was an Assistant Professor with the Institute of Communication, Information and Perception Technologies at the Scuola Superiore Sant' Anna, Pisa, Italy. From 2013 to 2015, he was an Assistant Professor of electrical and computer engineering (ECE) and materials with Boston University. In 2015, he joined the ECE Department, University of California Santa Barbara, where he is currently an Associate Professor. He is an Associate Editor for *Photonics Technology Letters* and the Vice Chair for the Microwave Theory and Techniques Society Subcommittee on Microwave Photonics. He was Program Chair for the Integrated Photonics Research, Silicon and Nanophotonics Conference in 2017, and is serving as General Chair for the same conference in 2018. He was the recipient of the best paper awards at the 2006 Conference on Optoelectronic and Microelectronic Materials and Devices and the 2007 Microwave Photonics Conference. He was also the recipient of a NASA Early Career Faculty Award. He is a Senior Member of OSA.